Leontaritis, A., Nassehi, A., & Yon, J. M. (2020). A Monte-Carlo Analysis of the Effects of Geometric Deviations on the Performance of Magnetic Gears. *IEEE Transactions on Industry Applications*, *56*(5), 4857-4869. https://doi.org/10.1109/tia.2020.3008115

# A Monte-Carlo Analysis of the Effects of Geometric Deviations on the Performance of Magnetic Gears

Alexandros Leontaritis
*Electrical Energy Management Group*
*Faculty of Engineering*
*University of Bristol*
United Kingdom
a.leontaritis@bristol.ac.uk

Aydin Nassehi
*Engineering Systems and Design Group*
*Faculty of Engineering*
*University of Bristol*
United Kingdom
aydin.nassehi@bristol.ac.uk

Jason Yon
*Electrical Energy Management Group*
*Faculty of Engineering*
*University of Bristol*
United Kingdom
jason.yon.02@bristol.ac.uk

***Abstract*— Magnetic gears offer several advantages over mechanical transmissions. However, across a broad range of research studies, their practical performance has not matched design predictions. Even with extensive 3D Finite Element Analysis (FEA), large discrepancies of 4% to 10% can exist – usually attributed to manufacturing error. Research studies typically assume ideal realization of the prototype geometry while employing basic, poorly characterized manufacturing processes in the hardware development. Geometric deviations due to manufacturing error are difficult to predict and inherently random. Therefore, their effect needs to be assessed through a statistical approach, which requires a rapid but accurate model of the gear. This paper assesses the effect of geometric error on the performance of a magnetic gear using a new computationally efficient asymmetric analytical model to conduct a Monte-Carlo simulation. The analytical technique is validated by comparing the results with a finite element solution and very close agreement is observed. By repeatedly analyzing the gear, with the position and size of each pole piece independently varied each time, a resultant distribution of performance can be derived. It is also shown that, for this case study, the distribution derived using the analytical model can be scaled to match the equivalent, but much more computationally onerous, FEA based solution. A predicted statistical distribution of a gear's performance, based on a set of manufacturing tolerances, would provide designers with a more realistic estimate of a gear's capability than an idealized analysis. This will be increasingly important as magnetic gears become more widely adopted.**

***Keywords—Magnetic gears, asymmetric analytical method, geometric deviation, manufacturing error, Monte-Carlo***

## I. INTRODUCTION

Many engineering applications require a multiplication of either angular speed or torque, and there is a wide range of transmission systems which can be used for this purpose. Mechanical gears are a highly developed technology which dominates the transmission sector of many engineering applications. However, the mechanical contact between the gears creates some fundamental drawbacks, including friction-induced wear and vibrations, increased maintenance requirements and reduced reliability. Since the beginning of the 21st century, Magnetic Gears (MGs) have received increased attention due to their contactless nature, low maintenance requirements and inherent overload protection. Researchers have also shown torque densities exceeding 100 kNm/m$^3$ can be achieved; comparable to two and three stage helical gearboxes [1]. They are therefore considered as promising alternatives in applications ranging from electrified vertical takeoff vehicles to tidal turbines and small-scale robotics [2]–[4].

There is a substantial body of work in the literature investigating a number of different topologies, including coaxial, harmonic and planetary MGs [5]–[13]. Such research projects typically concentrate on the optimization of the gear for a particular performance metric, with much of the literature focusing on torque density. The most common analysis method for MGs is Finite Element Analysis (FEA). However, there are numerous examples in the literature where a discrepancy is observed between FEA and experimental outcomes. Two-dimensional (2D) FEA is frequently used as it offers accessibility and gives a reasonable indication of performance. In studies using 2D FEA, large discrepancies can be observed ranging from 20% to 40% [10], [14], [15]. These are attributed to some combination of end-effects and manufacturing error. Three-dimensional (3D) FEA is significantly more computationally intensive but, can be employed to overcome the inherent limitations of 2D planar models. This can include the modelling of end effects and allow the influence of supporting structures to be assessed. However, as shown in [15], for the analysis of Coaxial Magnetic Gears (CMGs) (Fig. 1), knowledge of the aspect ratio allows compensation to be applied to 2D results with very good correlation to those obtained using 3D FEA. Even so, 3D FEA can still give a discrepancy of 4% to 10% [16]–[19]. In particular, in [19], 3D FEA is used and the end-effects due to almost all the supporting structures are considered, in addition to those of the active components. In this study a discrepancy of 9% is reported, which is attributed to "manufacturing error".

Despite extensive research studies, very few MGs can be found in the transmission industry. The reasons for this are unclear but, accurate techniques for predicting real-world performance will be essential for widespread adoption. MGs implemented in real-world applications would require a more wholistic design approach having to consider a wide range of characteristics including electromagnetic performance, thermal management, structural requirements and cost. The design philosophy must also be suited to scalable production processes. In particular, large scale production is only viable if the range in expected performance of the product can be predicted and deemed acceptable.

Calculated performance in research studies typically assumes exact geometry. Therefore, the effects of geometric imperfections are rarely considered. These imperfections are effectively a combination of geometric deviations due to manufacturing error and deflection of components under

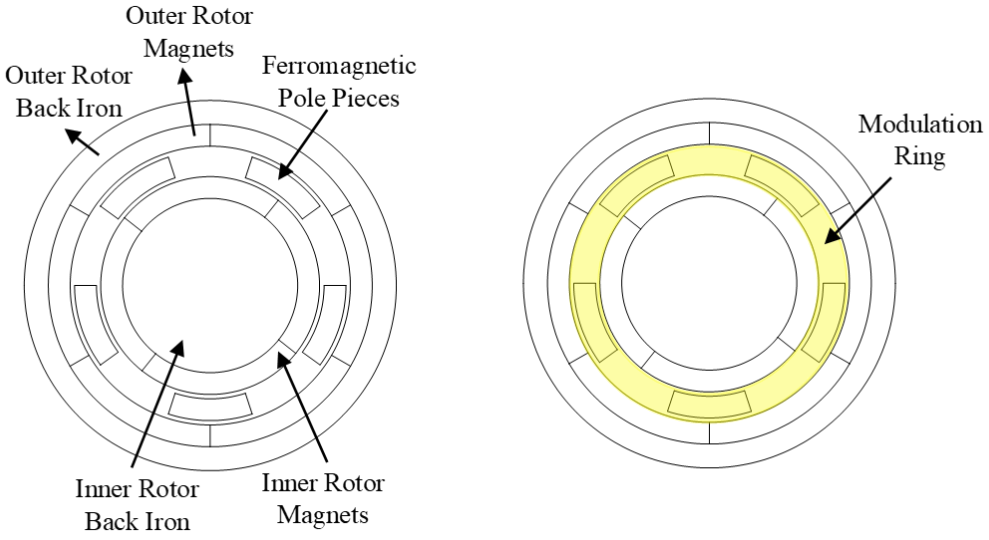


Fig. 1. CMG component identification

load [20]. This may be confounded by the fact that practical development of research machines is typically undertaken in a prototyping environment where manufacturing and assembly controls are basic. Consideration of the effect of geometric deviations can lead to better estimation of the expected performance and, in cases where deflections can be calculated, better correlation between modelling and prototypes.

This paper presents an analysis of the effects of geometric deviations on the performance of a CMG (illustrated in Fig. 1 with parameters outlined in Table I). This study focuses on geometric deviations in the modulation ring which are expected to be most significant [20]. The effects are assessed through a Monte-Carlo analysis for which an efficient and accurate analysis method is required. FEA, due to its high dependency on the mesh form, requires very high mesh density and, as a result, becomes computationally expensive and impractical for such a study [21]. Therefore, an asymmetric analytical subdomain model has been developed considering individual radial and tangential deviations of each ferromagnetic pole piece.

## II. Asymmetric Analytical Model

In the literature, analytical models for CMGs have been developed using solutions of the magnetic vector potential ($A$) [22]–[27]. However, these assume radial symmetry for each of the three main components (the two PM rotors and the modulation ring) and are therefore only able to model simple bulk geometric errors, such as incorrect radii. More realistic geometric deviations are inherently asymmetric and cannot be considered with the models mentioned above.

In [28], Pina et. Al presented an asymmetric analytical model of a permanent magnet machine, which allowed efficient analysis of rotor and stator asymmetries. With this they were able to study the effect of manufacturing error on cogging torque. Following their approach, in [21] Leontaritis et. Al presented an initial asymmetric model of a CMG, however this model considered only tangential deviation of each pole piece and radial deviation of each PM. In [20] it was concluded that realistic deviation of the modulation ring pole pieces in $r$ and $\theta$ is likely to be a more significant source of error than incorrect rotor geometry. This stems from the fact that PM rotors are now a relatively mature technology and their manufacturing processes are likely to be relatively well controlled – even in research prototypes.

Here an analytical model is presented that allows the size and position of each pole piece to be deviated, emulating realistic manufacturing error in the modulation ring. In common with [21], the CMG is separated into concentric regions (Fig. 2) and the modulation ring is divided further into angular subdomains equal to the number of pole pieces (Q). However, to account for the asymmetries in the radial and tangential position of each pole piece, careful treatment of the boundary conditions is required. Here the air-gaps are also divided into angular subdomains to match the modulation ring. Each region II subdomain is now bounded to its equivalent subdomain of region III. The full set of boundary conditions is given in (15) – (22). The following assumptions are also applied:

- $A$ is a function of $r$ and $\theta$ and only has a vector component in the z-direction;
- Infinite permeability is applied to the ferromagnetic regions;
- The PMs are assumed to be linear and have unity relative permeability;
- End effects are neglected.

TABLE I. CMG Parameters

| Quantity | Value |
|---|---|
| Number of pole pieces ($Q$) | 5 |
| Inner rotor poles ($P_{in}$) | 4 |
| Outer rotor poles ($P_{out}$) | 6 |
| Inner rotor OD | 100 mm |
| Outer rotor OD | 148 mm |
| Axial Length | 100 mm |

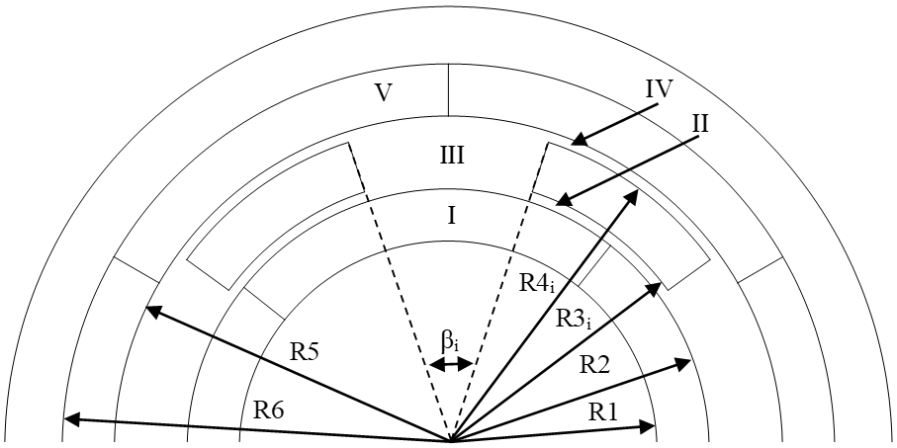


Fig. 2. Definition of regions, radii and slot angle

The magnetic vector potential in each region can be calculated by solving Poisson's equation and Laplace's equation in the PM and non-magnetized regions, respectively. The general solutions have been simplified by adopting the following notations:

$$U_z(a,b) = \left(\frac{a}{b}\right)^z + \left(\frac{b}{a}\right)^z \tag{1}$$

$$Q_z(a,b) = \left(\frac{a}{b}\right)^z - \left(\frac{b}{a}\right)^z \tag{2}$$

Using the separation of variables method, the general solution for each region can be derived. The solutions, described by Fourier series, are provided in (3), (4), (11) – (13). In the rotor PM regions (I, V) the general solutions are as follows:

$$\begin{aligned} A^{(I)}(r,\theta) = &\sum_{k=1}^{K}\left(W_{1k}C_I + W_{2k}M_{rck}^{(I)}\right)\cos(k\theta) \\ &+ \sum_{k=1}^{K}\left(W_{1k}E_I + W_{2k}M_{rsk}^{(I)}\right)\sin(k\theta) \end{aligned} \tag{3}$$

$$\begin{aligned} A^{(V)}(r,\theta) = &\sum_{k=1}^{K}\left(W_{3k}C_V + W_{4k}M_{rck}^{(V)}\right)\cos(k\theta) \\ &+ \sum_{k=1}^{K}\left(W_{3k}E_V + W_{4k}M_{rsk}^{(V)}\right)\sin(k\theta) \end{aligned} \tag{4}$$

where

$$W_{1k} = \frac{U_k(r,R_1)}{U_k(R_2,R_1)} \tag{5}$$

$$\begin{aligned} w_{2k} = &\left[1 + \frac{1}{k}\left(\frac{R_1}{r}\right)^{k+1}\right]\cdot r \\ &- \frac{U_k(r,R_1)}{U_k(R_2,R_1)}\left[1 + \frac{1}{k}\left(\frac{R_1}{R_2}\right)^{k+1}\right]\cdot R_2 \end{aligned} \tag{6}$$

$$W_{3k} = \frac{U_k(r,R_6)}{U_k(R_5,R_6)} \tag{7}$$

$$\begin{aligned} W_{4k} = &\left[1 + \frac{1}{k}\left(\frac{R_6}{r}\right)^{k+1}\right]\cdot r \\ &- \frac{U_k(r,R_6)}{U_k(R_5,R_6)}\left[1 + \frac{1}{k}\left(\frac{R_6}{R_5}\right)^{k+1}\right]\cdot R_5 \end{aligned} \tag{8}$$

and

$$M_{rck}^{(I,V)} = \frac{2PB_{rm}}{k\pi\mu_0} sin\left(\frac{k\pi\alpha_p}{P}\right) cos(k\varphi_0) \tag{9}$$

$$M_{rsk}^{(I,V)} = \frac{2PB_{rm}}{k\pi\mu_0} sin\left(\frac{k\pi\alpha_p}{P}\right) sin(k\varphi_0) \tag{10}$$

for $k/P = 1, 3, 5, \ldots$

Each general solution is bounded by the inner ($R_1$, $R_5$) and outer ($R_2$, $R_6$) radii of each PM region. The parameter $k$ denotes the order of harmonics in each region, with $B_{rm}$ being the residual flux and $P$, $\mu_o$, $\alpha_p$ are the number of poles, the permeability of free space and the magnet arc to pole pitch ratio, respectively. The terms $C_I$ and $E_I$ are Fourier coefficients. The initial angular position of the rotor is defined by $\varphi_o$.

Similarly, the general solution for each air-gap subdomain (II, IV) and the pole-pieces region (III) can be described as:

This research has been funded by the Engineering and Physical Sciences Research Council (EPSRC).

$$A_i^{(II)}(r,\theta) = \sum_{k=1}^{K}\left(C_{II,\mathrm{i}}\frac{R_2}{k}\frac{U_k(r,R_{3,\mathrm{i}})}{Q_k(R_2,R_{3,\mathrm{i}})} + D_{II,\mathrm{i}}\frac{R_{3,\mathrm{i}}}{k}\frac{U_k(r,R_2)}{Q_k(R_{3,\mathrm{i}},R_2)}\right)\cos(k\theta) + \sum_{k=1}^{K}\left(E_{II,\mathrm{i}}\frac{R_2}{k}\frac{U_k(r,R_{3,\mathrm{i}})}{Q_k(R_2,R_{3,\mathrm{i}})} + F_{II,\mathrm{i}}\frac{R_{3,\mathrm{i}}}{k}\frac{U_k(r,R_2)}{Q_k(R_{3,\mathrm{i}},R_2)}\right)\sin(k\theta) \quad (11)$$

$$A_i^{(IV)}(r,\theta) = \sum_{k=1}^{K}\left(C_{IV,\mathrm{i}}\frac{R_{4,\mathrm{i}}}{k}\frac{U_k(r,R_5)}{Q_k(R_{4,\mathrm{i}},R_5)} + D_{IV,i}\frac{R_5}{k}\frac{U_k(r,R_{4,\mathrm{i}})}{Q_k(R_5,R_{4,\mathrm{i}})}\right)\cos(k\theta) + \sum_{k=1}^{K}\left(E_{IV,\mathrm{i}}\frac{R_{4,\mathrm{i}}}{k}\frac{U_k(r,R_5)}{Q_k(R_{4,\mathrm{i}},R_5)} + F_{IV,i}\frac{R_5}{k}\frac{U_k(r,R_{4,\mathrm{i}})}{Q_k(R_5,R_{4,\mathrm{i}})}\right)\sin(k\theta) \quad (12)$$

$$A_i^{(III)}(r,\theta) = C_{III,i} + D_{III,i}\ln(r) + \sum_{m=1}^{M}\left(E_{III,i,m}\frac{Q_{f_{m,i}}(r,R_{4,s})}{Q_{f_{m,i}}(R_{3,s},R_{4,s})} - F_{III,i,m}\frac{Q_{f_{m,i}}(r,R_{3,s})}{Q_{f_{m,i}}(R_{3,s},R_{4,s})}\right)\cdot\cos\left(f_{m,i}(\theta-\theta_i)\right) \quad (13)$$

with

$$f_{m,i} = \frac{m\pi}{\beta_i} \quad (14)$$

where $m$ defines the order of harmonics and $\beta_i$, $\theta_i$ are the opening angle and angular position of the i[th] slot between consecutive pole pieces and $s$ is equal to $i$ or $i$-$1$ depending on the matching of pole pieces and slots in the clockwise or anticlockwise directions. The terms $C_{II,\mathrm{i}}$, $D_{II,\mathrm{i}}$, $E_{II,\mathrm{i}}$ and $F_{II,\mathrm{i}}$ are Fourier coefficients.

Each air-gap subdomain solution is calculated for the [0, 2π] angular domain. The complete solution in the air-gap can then be constructed by using the appropriate subdomain for the angular region it occupies (Fig. 3). This fact, in addition to the continuity of the radial component of the flux density and the tangential component of the field intensity leads to the following boundary equations that are used to define the expressions at each interface:

$$H_\theta^{(I)}\big|_{r=R_2} = H_{\theta,\mathrm{i}}^{(II)}\big|_{r=R_2} \quad (15)$$

$$B_r^{(I)}\big|_{r=R_2} = B_{r,\mathrm{i}}^{(II)}\big|_{r=R_2} \quad (16)$$

$$H_{\theta,i}^{(II)}\big|_{r=R_{3,\mathrm{i}}} = H_\theta^{(III)}\big|_{r=R_{3,\mathrm{i}}} \quad (17)$$

$$A_i^{(II)}\big|_{r=R_{3,\mathrm{i}}} = A_i^{(III)}\big|_{r=R_{3,\mathrm{i}}} \quad (18)$$

$$H_\theta^{(III)}\big|_{r=R_{4,\mathrm{i}}} = H_{\theta,i}^{(IV)}\big|_{r=R_{4,\mathrm{i}}} \quad (19)$$

$$A_i^{(III)}\big|_{r=R_{4,\mathrm{i}}} = A_i^{(IV)}\big|_{r=R_{4,\mathrm{i}}} \quad (20)$$

$$H_{\theta,\mathrm{i}}^{(IV)}\big|_{r=R_5} = H_\theta^{(V)}\big|_{r=R_5} \quad (21)$$

$$B_{r,\mathrm{i}}^{(IV)}\big|_{r=R_5} = B_r^{(V)}\big|_{r=R_5} \quad (22)$$

Applying the boundary equations (15) – (22) to the general solutions in each subdomain (3), (4), (11) – (13) the complete solution can be derived and expressed in matrix form as in (23).

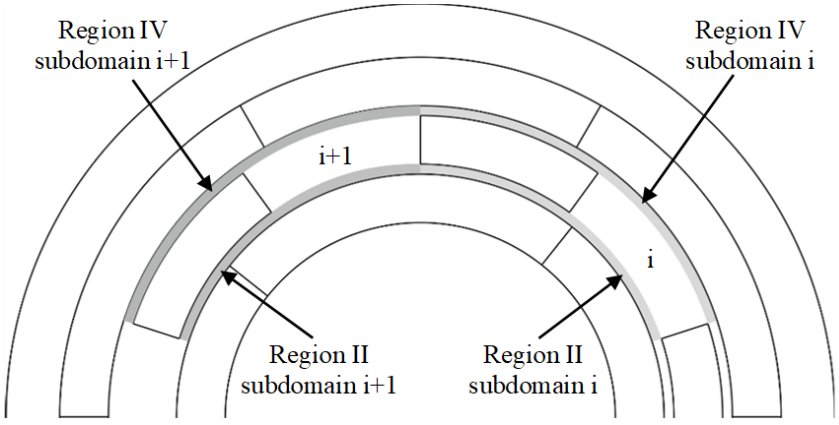


Fig. 3. Angular regions occupied by the air-gap subdomain

TABLE II. PARAMETER ERROR FOR MODEL VALIDATION

| Variable | Pole Piece Error | | | | |
|---|---|---|---|---|---|
| | ***No. 1*** | ***No. 2*** | ***No. 3*** | ***No. 4*** | ***No. 5*** |
| Length (mm) | 0.018 | -0.014 | 0.001 | -0.020 | -0.019 |
| Angular arc (deg) | 0.019 | -0.018 | 0.001 | 0.009 | 0.018 |
| Radial position (mm) | -0.001 | 0.204 | -0.103 | 0.050 | -0.030 |
| Angular position (deg) | 0.206 | 0.011 | -0.199 | -0.099 | -0.142 |

$$\boldsymbol{X} \cdot \boldsymbol{K} = \boldsymbol{Y} \tag{23}$$

where $\boldsymbol{K}$ is a column matrix containing all the unknown Fourier coefficients of each general solution. The supplementary matrices $\boldsymbol{X}, \boldsymbol{Y}$ are defined through algebraic manipulation. This analytical solution is presented in more detail in Appendix A.

### *A. Analytical Model Validation*

The accuracy of the analytical model is assessed by comparing a solution of a sample deviated gear to a 2D finite element analysis of the same geometry. For the purpose of this study, a degree of error has been arbitrarily introduced to the two dimensions and radial and tangential position of each pole piece. This error is recorded in Table II. For each region the first 200 harmonics were considered. The field solution shows excellent correlation with FEA results (Fig. 4), under the same infinite permeability assumption. The FEA software used in this analysis is FEMM [29]. The mesh density in the FE model was set using the approach outlined in [21].

The computational efficiency of this approach depends on the number of harmonics used. The consideration of higher-order harmonics can increase the accuracy of the model; however, this comes at the expense of computational time. The relationship between the number of harmonics and the accuracy and speed of the model is shown in Fig. 5. It is observed that the analytical torque results converge to the FEA after the first 50 harmonics. For the purpose of the Monte-Carlo analysis, the first 100 harmonics are considered, as the simulation samples will differ slightly to the sample model of Fig. 4. The computational time of the model with the selected harmonics is 2.9 s, more than an order of magnitude faster than the equivalent FEA. It must be noted the relationship between speed and number of harmonics is unique for each CMG. CMGs with higher number of poles, and hence higher number of pole pieces, will increase the computational time. Therefore, harmonic selection methods

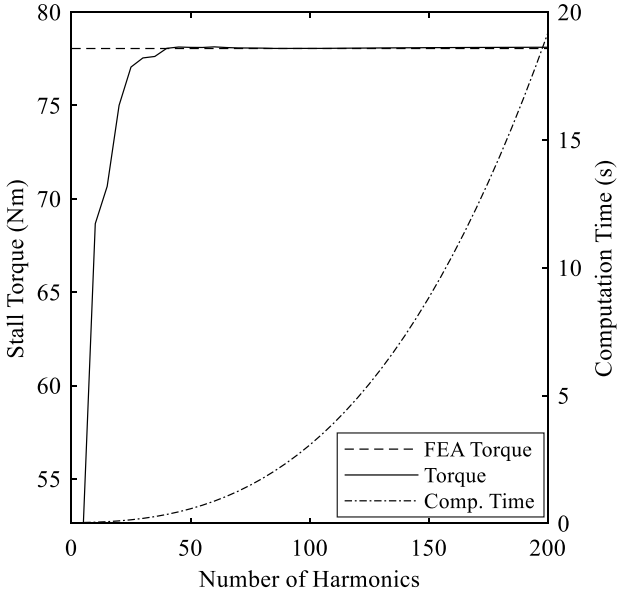


Fig. 5. Model harmonics vs accuracy and speed for sample CMG

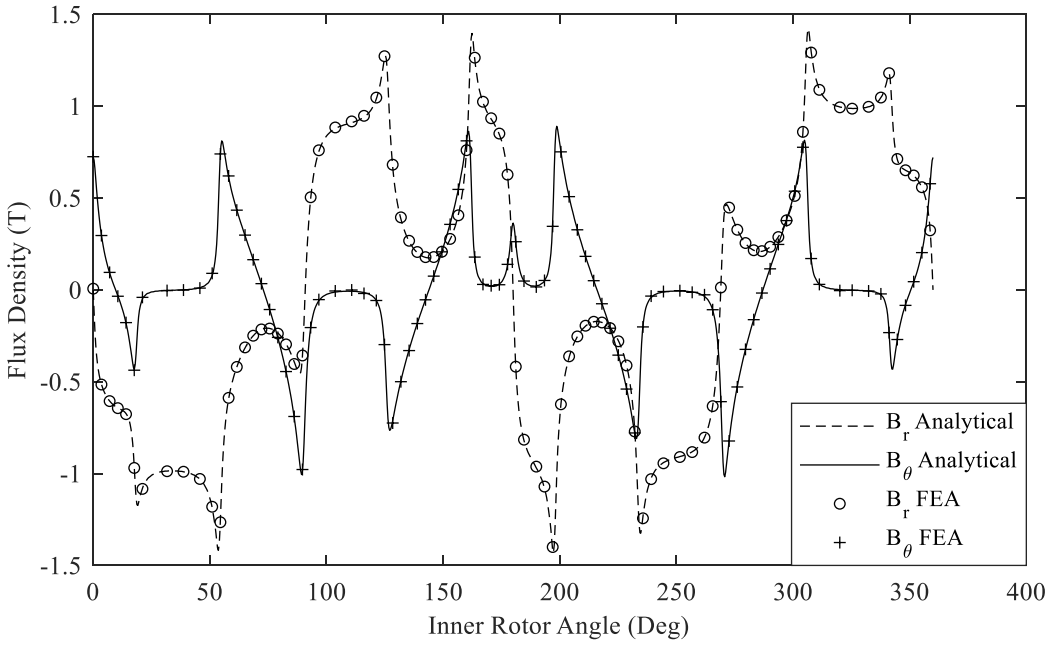


Fig. 4. Analytical vs FEA flux density comparison, assuming infinite permeability

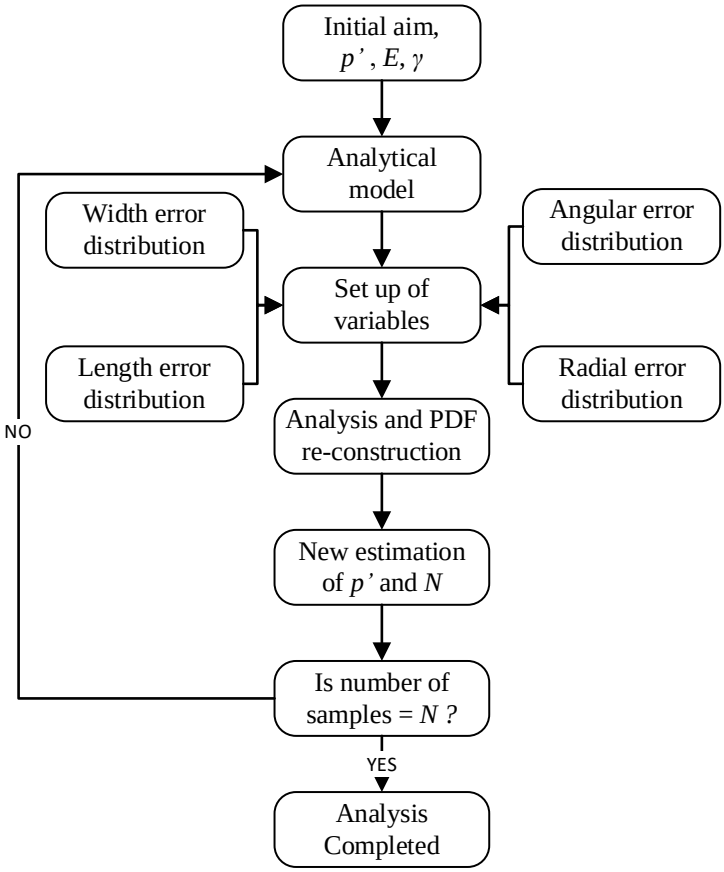


Fig. 6. Process diagram of the Monte-Carlo analysis

such as the ones presented in [27], [30] may be required to speed up the model.

## III. Monte Carlo Analysis

In a mass production environment, defining the acceptable range of product performance is as important as calculating ideal performance. Manufacturing tolerances are then specified to achieve an economically acceptable probability of a specific product falling into this range. The stochastic nature of manufacturing error means assessment of its effect requires the use of statistical methods. The range of outputs from a manufacturing process can be described through a Probability Density Function (PDF) of the desired performance variable. In cases where the PDF is unknown, PDF estimators can be used in conjunction with a number of samples to construct the PDF.

In this study the effect of geometric deviation of the pole pieces of a CMG is discerned through a Monte-Carlo analysis. A group of deviated samples is analyzed, each employing a different set of parameters. The parameters considered are the radial and angular position along with the length and angular arc of each pole piece. For each simulation the value of each parameter is obtained through random sampling of their respective distribution. It is assumed that the manufacturing error in the dimensions of the pole pieces is normally distributed [28]. In [20] the expected tolerances with respect to a selected manufacturing process are provided. A tolerance of 0.05 mm has been selected as the three-sigma value for the respective distribution, which corresponds to stamping and Electric Discharge Machining (EDM). The position of the pole pieces is affected by errors in manufacture and assembly but also by deflection due to magnetic forces within the gear. Assessing the distribution of pole piece position is therefore much more complicated than pole piece dimensions. This deflection due to magnetic forces is highly dependent on the mechanical properties of the pole pieces themselves and their supporting structure. Furthermore, as the pole pieces deflect, they will experience new magnetic loads which lead to further deflections [20], [31]. Proper assessment of this is likely to require an iterative solution such as [31] and can only be meaningfully undertaken with a full mechanical design. Therefore, for the purpose of this study, the position distributions have also been assumed to be normally distributed with a three-sigma value of 0.4 mm for the radial error and 0.4 deg for the tangential error. These values are similar to the positional error reported in [31], [32].

A PDF can be estimated using parametric or nonparametric methods. Nonparametric methods are well suited to cases where there is insufficient information regarding the profile of the PDF, whereas parametric estimators initially assume an underlying PDF form [33]. The estimator used in this study is the Kernel Density Estimator (KDE) which is a nonparametric method approximating the true PDF at discrete points rather than volumetrically. The KDE formula is defined in (24):

$$\hat{f}_h(x) = \frac{1}{Nh}\sum_{i=1}^{N} k\left(\frac{x - x_i}{h}\right) \tag{24}$$

TABLE III. PARAMETERES FOR MONTE CARLO ANALYSIS

| Parameter | Value | Distribution |
|---|---|---|
| ***Tolerance*** | | |
| Length (mm) | 0.05 | Normal |
| Angular arc (deg) | 0.05 | Normal |
| Radial position (mm) | 0.4 | Normal |
| Angular position (deg) | 0.4 | Normal |
| ***Statistical Parameters*** | | |
| $E$ | 0.01 | N/A |
| $z$ | 1.96 | N/A |
| Initial $p'$ | 0.5 | N/A |

where $x_1, \ldots, x_N$ are the samples of the unknown distribution, $h$ is the bandwidth and $k$ is the user-defined kernel function. The properties of $k$ are provided in (25) [33]

$$\int k(u)du = 1, \quad \int uk(u)\,du = 0, \quad \int u^2 k(u)du = k_2 \neq 0 \tag{25}$$

The bandwidth has a significant effect on the results of the KDE. In the literature, an optimal bandwidth has been reported which minimizes the Mean Integrated Square Error (MISE) [34]. The KDE is obtained through the KDE function in Matlab [35], which uses (24) with the optimal bandwidth calculated from (26) [36].

$$h = \left(\frac{4}{3N}\right)^{\frac{1}{5}} \sigma \tag{26}$$

where σ is an initial estimate of the standard deviation of $\hat{f}_h(x)$ and is calculated as in [36]. The Epanechnikov kernel [37], which is also known to minimize the MISE according to the properties in (25) [33], has also been used throughout this study.

The last important factor of the Monte-Carlo analysis is the number of samples. The larger the number of samples, the better the correlation will be between the simulated and true PDFs. However, this comes at a cost of increasing computational time. Equation (27) is provided in [38] as a mean of calculating the required number of samples when investigating the probability of an "event". Therefore, computational efficiency is maximized.

$$N = \frac{p'(1-p')}{E^2} z^2_{(1+\gamma)/2} \tag{27}$$

where $p'$ is an estimate of the probability, $E$ is the allowable error in the estimation of $p'$, $\gamma$ represents the confidence interval and $z_a$ is the 100(α) percent point of a standard normal distribution [38].

The process diagram of the Monte-Carlo analysis is shown in Fig. 6. Initially, the aim is set and the statistical parameters $p'$, $E$ and $\gamma$ are selected. An initially conservative $p'$ of 0.5 is set and the value of each variable is obtained from their respective distributions. A solution is then calculated from the analytical model in Section II and a value of the stall torque is obtained. This is normalized with respect to the nominal torque of a non-deviated CMG. Using the KDE the PDF is re-constructed and a better estimate of $p'$ is obtained. The required number of samples is then updated automatically according to (27) and, when reached, the simulation is completed. For validation and comparison purposes the same Monte-Carlo analysis is performed in FEMM and the two results are discussed in Section IV.

## IV. RESULTS

For the purpose of this study, an initial aim was set to determine the probability of a sample achieving an inner rotor stall torque within ± 1% of the nominal. The acceptable error $E$ was set to 0.01 and the 95% confidence interval was selected, leading to a $z$ value of 1.96. The complete set of parameters of the analysis is provided in Table III. Two scenarios were considered; a standard and a "poorly manufactured" case, where the stated tolerance corresponds to the three-sigma and two-sigma values, respectively. For each case, a Monte-Carlo simulation was performed using three modelling techniques: non-linear FEA; linear FEA assuming infinite permeability in the iron regions and the analytical model.

The Monte-Carlo simulation for the standard case was completed according to Fig. 6 and 7545 samples were required. The total computational time using the analytical solution was approximately 7.3 hours using a computer with the following specifications: Intel(R) Core(TM) i7-6700 CPU @ 3.40GHz, 16 GB RAM. In comparison, the linear FEA took approximately 150 hours, with the more computationally heavy non-linear FEA requiring around 480 hours to complete. Consequently, the latter was completed by operating 30 computers of the same specification concurrently for approximately 16 hours.

The results of each of the three analysis methods are shown in their re-constructed Cumulative Distribution Function (CDF) plots of Fig. 7 and Fig. 8. Considering the standard case (Fig. 7), the CDF shows good correlation between the analytical solution and the linear FEA. However, both linear analyses give a more conservative distribution (i.e.

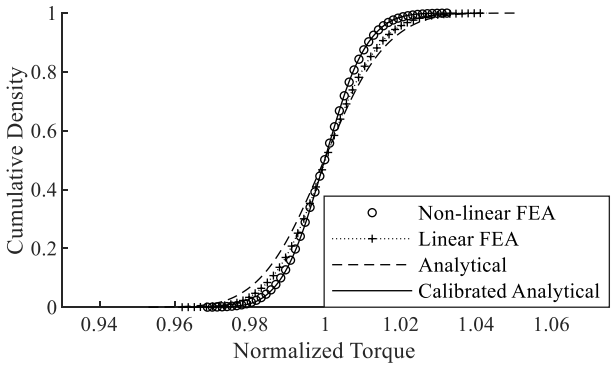


Fig. 7. Analytical vs FEA comparison CDF – Standard case

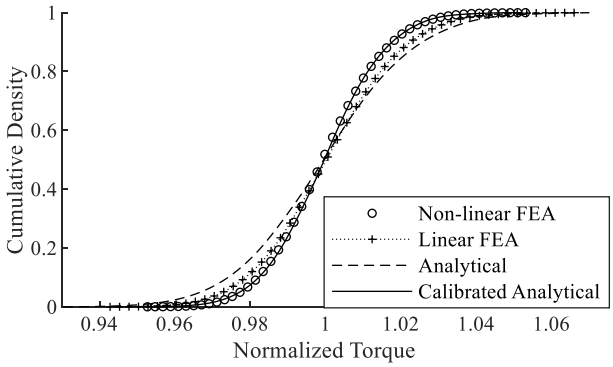


Fig. 8. Analytical vs FEA comparison CDF – Poorly manufactured case

it predicts a higher probability of poor performance) than the non-linear FEA. This is even more pronounced for the poorly manufactured case.

However, when comparing stall torque results for a specific gear instance (i.e. a defined set of geometric deviations) calculated using the analytical model and non-linear FEA, a linear trend can be observed. This indicates that a scaling factor could be applied to calibrate the analytical results. Fig. 9 shows the normalised stall torque results for 115 gear instances using both types of analysis. A line of fit can be applied through the central point (1,1) and the gradient of this line can then be used to scale results of the analytical model as a function of the stall torque.

From Fig. 7 and Fig. 8 it is evident that excellent correlation is achieved between the calibrated analytical and the non-linear FEA with only a small number of FEA solutions required for the calibration. This translates into very similar results in the calculation of the probability *p'* (Table IV), the initial aim of this section.

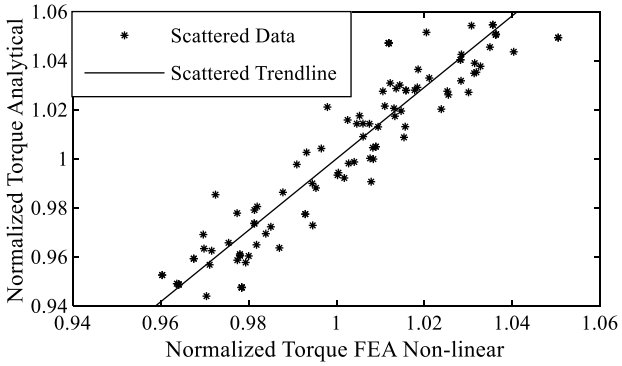


Fig. 9. Analytical calibration – Poorly manufactured case

TABLE IV. PARAMETERES FOR MONTE CARLO ANALYSIS

| **Standard Case** | | | | |
|---|---|---|---|---|
| | ***Analytical*** | ***Linear FEA*** | ***FEA*** | ***Calibrated Analytical*** |
| ***p'*** | 0.58 | 0.61 | 0.73 | 0.73 |
| **Poorly manufactured Case** | | | | |
| | ***Analytical*** | ***Linear FEA*** | ***FEA*** | ***Calibrated Analytical*** |
| ***p'*** | 0.40 | 0.45 | 0.53 | 0.53 |

## V. DISCUSSION

The nature of stochastic manufacturing variations in a complex system makes experimental validation of probable performance impractical. However, fast and accurate models allow a large number of products, each with unique manufacturing errors, to be simulated so that a distribution of product performance can be predicted.

The analytical model has been shown to be very computationally efficient but conservative in overestimating the probability of poor performance when compared to FEA. On the other hand, while non-linear FEA is in practice too slow to complete Monte-Carlo studies of this nature, it does precisely model subtleties of geometry and material non-linearity. A hybrid approach is clearly the ideal solution combining the accuracy of FEA and computational efficiency of the analytical model. This way, even if the raw data from the analytical model overestimates the effect of manufacturing error (compared with the FEA), the results can be easily calibrated using a small number of FEA solutions. Thus, accuracy and computational efficiency are both maximized.

Considering the results of the study, the extent to which geometric deviations can affect the stall torque of the CMG is related to how well the manufacturing processes are controlled. From Fig. 7 and Fig. 8 it is clear that poorly controlled manufacturing processes substantially widen the cumulative density function. For the well-manufactured case, approximately 1.5% of the gear instances have a stall torque more than 2% lower than the nominal. For this design with these manufacturing tolerances, a relatively modest safety factor could ensure that virtually all gears meet the required performance. However, if manufacturing processes are not well controlled, the situation worsens. This can be seen in Fig. 8 with 7.5% of gear instances having a stall torque more than 2% lower than the nominal.

It is likely that the methods outlined in this study could be equally applied to similar gear designs. However, the number of FEA studies required to ensure an accurate calibration needs to be considered. This could relate to both the underlying manufacturing distributions and the specific gear parameters. In addition, further work would be required to apply an asymmetric model of this type to other gear topologies - for example those where a permeable mechanical bridge exists between adjacent pole pieces [39]. A general conclusion on the applicability of this method would probably require a large sample of CMGs of different types to be analyzed.

To relate this work to discrepancies in gear performance reported in the literature, specific knowledge of the manufacturing processes for each case would be required, along with enough evidence to predict the relevant underlying distributions. As outlined earlier, practical development of research machines is typically undertaken in a prototyping

environment with limited controls on manufacturing and assembly error. These underlying distributions could therefore be much worse that those considered in this study.

In addition to manufacturing error, geometric deviations caused by deflections of the structure under its own magnetic loads will also have an effect. These deflections are a more complex consideration than manufacturing error as it would be difficult to accurately approximate this effect by assuming an underlying distribution. As stated in Section III and in [31], calculating deflections is likely to require an iterative process linking a mechanical model with an electromagnetic simulation. If these calculations could be performed with comparable efficiency to the model presented in this paper, the compounding effects of manufacturing error and deflection of the structure could be assessed in similar statistical studies.

In terms of performance of the analytical model itself, it can be observed that the correlation with both linear and non-linear FEA deteriorates for gear instances with large geometric deviations. While this can be calibrated as demonstrated here for a statistical analysis, this observation may suggest that there are limits to the approximation of an asymmetric problem using Fourier Series. Further research to quantify this limitation is certainly warranted.

## VI. Conclusions

Statistical analysis of the effect of manufacturing errors in complex products requires fast and accurate models. This study has developed and verified a statistical method using a novel asymmetric analytical model to calculate the effects of geometric deviations on the performance of CMGs. A complete methodology has been demonstrated and several conclusions and indications for further study have been drawn from the results.

The new analytical model can simulate realistic asymmetric variations in the modulation ring; previously found to be the most susceptible region for geometric error. It is flexible and computationally efficient and can therefore be used as part of a Monte-Carlo analysis. A balanced approach has been demonstrated using the analytical model to develop the output distribution profile and a small number of FEA solutions to calibrate the results. This maximizes both accuracy and computational efficiency. The set of statistical techniques employed is as important as the system model. In a study such as, this the resultant PDF is always an unknown. The Kernel Density Estimator, which does not assume a parametric distribution, has been shown to be well-suited to this task.

Close correlation has been achieved between the CDFs developed using the calibrated analytical model and non-linear FEA – with calibration in this case being achieved with only 115 data pairs. The methods presented in this paper provide a practicable means to assess the effect of manufacturing processes, and their errors, on CMG performance.

## Authors

**Alexandros Leontaritis** received the M.Eng. degree in Mechanical Engineering from the Department of Mechanical Engineering, University of Bristol, Bristol, U.K., in 2017. He is currently working toward the PhD degree with the Electrical Energy Management Group, Faculty of Engineering, University of Bristol.

**Aydin Nassehi** is a Reader in Manufacturing Systems and Head of the Department of Mechanical Engineering, University of Bristol. He received his PhD in Innovative Manufacturing Technology from the University of Bath, Bath, U.K. in 2007. His research interests are in modelling and analysis at manufacturing systems and informatics and artificial intelligence in manufacturing.

**Jason M. Yon** received the MEng degree in Avionic Systems Engineering in 2007 and a PhD in Aerospace Electrical Systems in 2012, both from the University of Bristol. He is now a Lecturer in Electromechanical Systems at the University of Bristol. His research covers a broad range of topics related to electric machines, design and manufacture and the development of novel characterization techniques for electromechanical systems.

## APPENDIX

### A. Asymmetric Analytical Model

The analytical method is based on solutions of the magnetic vector potential (*A*). These solutions reduce to the Laplace's and Poisson's equations using magnetic flux density (*B*), which is the curl of *A* (A-1), and Maxwell's Ampere law equation (A-2).

$$\vec{B} = \nabla \times \vec{A} \tag{A-1}$$

$$\nabla \times \vec{B} = \mu_0 \vec{J} + \mu_0 \varepsilon_0 \frac{\partial \vec{E}}{\partial t} \tag{A-2}$$

Since a magnetostatic solution is required, the partial derivative of the electric flux density (*E)* disappears. Furthermore, as there is no applied current, the current density (*J)* is given by the curl of the magnetization vector (*M*) in the PM regions and is zero elsewhere. Therefore, equations (A-1) and (A-2) lead to (A-3) in the PM regions and (A-4) in all other regions:

$$\nabla^2 \vec{A} = -\mu_0 \nabla \times \vec{M} \tag{A-3}$$

$$\nabla^2 \vec{A} = 0 \tag{A-4}$$

The general solutions of equations (A-3), (A-4), described by Fourier series, are provided in (A-7), (A-8), (A-15) – (A-17). These solutions have been simplified by adopting the notation in (A-5), (A-6).

$$U_z(a,b) = \left(\frac{a}{b}\right)^z + \left(\frac{b}{a}\right)^z \tag{A-5}$$

$$Q_z(a,b) = \left(\frac{a}{b}\right)^z - \left(\frac{b}{a}\right)^z \tag{A-6}$$

In the rotor PM regions (I, V) the general solutions are as follows:

$$\begin{aligned} A^{(I)}(r,\theta) = &\sum_{k=1}^{K} \left(W_{1k} C_I + W_{2k} M_{rck}^{(I)}\right) \cos(k\theta) \\ &+ \sum_{k=1}^{K} \left(W_{1k} E_I + W_{2k} M_{rsk}^{(I)}\right) \sin(k\theta) \end{aligned} \tag{A-7}$$

$$\begin{aligned} A^{(V)}(r,\theta) = &\sum_{k=1}^{K} \left(W_{3k} C_V + W_{4k} M_{rck}^{(V)}\right) \cos(k\theta) \\ &+ \sum_{k=1}^{K} \left(W_{3k} E_V + W_{4k} M_{rsk}^{(V)}\right) \sin(k\theta) \end{aligned} \tag{A-8}$$

where

$$W_{1k} = \frac{U_k(r,R_1)}{U_k(R_2,R_1)} \tag{A-9}$$

$$\begin{aligned} W_{2k} = &\left[1 + \frac{1}{k}\left(\frac{R_1}{r}\right)^{k+1}\right] \cdot r \\ &- \frac{U_k(r,R_1)}{U_k(R_2,R_1)}\left[1 + \frac{1}{k}\left(\frac{R_1}{R_2}\right)^{k+1}\right] \cdot R_2 \end{aligned} \tag{A-10}$$

$$W_{3k} = \frac{U_k(r,R_6)}{U_k(R_5,R_6)} \tag{A-11}$$

$$\begin{aligned} W_{4k} = &\left[1 + \frac{1}{k}\left(\frac{R_6}{r}\right)^{k+1}\right] \cdot r \\ &- \frac{U_k(r,R_6)}{U_k(R_5,R_6)}\left[1 + \frac{1}{k}\left(\frac{R_6}{R_5}\right)^{k+1}\right] \cdot R_5 \end{aligned} \tag{A-12}$$

and

$$M_{rck}^{(I,V)} = \frac{2PB_{rm}}{k\pi\mu_0} sin\left(\frac{k\pi\alpha_p}{P}\right) cos(k\varphi_0) \tag{A-13}$$

$$M_{rsk}^{(I,V)} = \frac{2PB_{rm}}{k\pi\mu_0} sin\left(\frac{k\pi\alpha_p}{P}\right) sin(k\varphi_0) \tag{A-14}$$

for $k/P = 1, 3, 5, \ldots$

Each general solution is bounded by the inner ($R_1$, $R_5$) and outer ($R_2$, $R_6$) radii of each PM region. The parameter *k* denotes the order of harmonics in each region, with $B_{rm}$ being the residual flux and *P*, $\mu_o$, $\alpha_p$ are the number of poles, the permeability of free space and the magnet arc to pole pitch ratio, respectively. The terms $C_I$ and $E_I$ are Fourier coefficients. The initial angular position of the rotor is defined by $\varphi_o$.

Similarly, the general solution for each air-gap subdomain (II, IV) and the pole-pieces region (III) can be described as:

$$\begin{aligned} A_i^{(II)}(r,\theta) = &\sum_{k=1}^{K} \left(C_{II,\mathrm{i}} \frac{R_2}{k} \frac{U_k(r,R_{3,\mathrm{i}})}{Q_k(R_2,R_{3,\mathrm{i}})} \right. \\ &\left. + D_{II,\mathrm{i}} \frac{R_{3,\mathrm{i}}}{k} \frac{U_k(r,R_2)}{Q_k(R_{3,\mathrm{i}},R_2)}\right) \cos(k\theta) \\ &+ \sum_{k=1}^{K} \left(E_{II,\mathrm{i}} \frac{R_2}{k} \frac{U_k(r,R_{3,\mathrm{i}})}{Q_k(R_2,R_{3,\mathrm{i}})} \right. \\ &\left. + F_{II,\mathrm{i}} \frac{R_{3,\mathrm{i}}}{k} \frac{U_k(r,R_2)}{Q_k(R_{3,\mathrm{i}},R_2)}\right) \sin(k\theta) \end{aligned} \tag{A-15}$$

$$A_i^{(IV)}(r,\theta)=\sum_{k=1}^{K}\left(C_{IV,\mathrm{i}}\frac{R_{4,\mathrm{i}}}{k}\frac{U_k(r,R_5)}{Q_k(R_{4,\mathrm{i}},R_5)}+D_{IV,i}\frac{R_5}{k}\frac{U_k(r,R_{4,\mathrm{i}})}{Q_k(R_5,R_{4,\mathrm{i}})}\right)\cos(k\theta)+\sum_{k=1}^{K}\left(E_{IV,\mathrm{i}}\frac{R_{4,\mathrm{i}}}{k}\frac{U_k(r,R_5)}{Q_k(R_{4,\mathrm{i}},R_5)}+F_{IV,i}\frac{R_5}{k}\frac{U_k(r,R_{4,\mathrm{i}})}{Q_k(R_5,R_{4,\mathrm{i}})}\right)\sin(k\theta) \quad \text{(A-16)}$$

$$A_i^{(III)}(r,\theta)=C_{III,i}+D_{III,i}\ln(r)+\sum_{m=1}^{M}\left(E_{III,i,m}\frac{Q_{f_{m,i}}(r,R_{4,s})}{Q_{f_{m,i}}(R_{3,s},R_{4,s})}-F_{III,i,m}\frac{Q_{f_{m,i}}(r,R_{3,s})}{Q_{f_{m,i}}(R_{3,s},R_{4,s})}\right)\cdot\cos\left(f_{m,i}(\theta-\theta_i)\right) \quad \text{(A-17)}$$

with

$$f_{m,i}=\frac{m\pi}{\beta_i} \quad \text{(A-18)}$$

where $m$ defines the order of harmonics and $\beta_i$, $\theta_i$ are the opening angle, angular position of the i$^{\text{th}}$ slot between consecutive pole pieces and $s$ is equal to $i$ or $i$-$1$ depending on the matching of pole pieces and slots in the clockwise or anticlockwise directions. The terms $C_{II,\mathrm{i}}$, $D_{II,\mathrm{i}}$, $E_{II,\mathrm{i}}$ and $F_{II,\mathrm{i}}$ are Fourier coefficients.

The boundary conditions at each interface are provided in (A-19) – (A-26).

$$H_\theta^{(I)}\big|_{r=R_2}=H_{\theta,\mathrm{i}}^{(II)}\big|_{r=R_2} \quad \text{(A-19)}$$

$$B_r^{(I)}\big|_{r=R_2}=B_{r,\mathrm{i}}^{(II)}\big|_{r=R_2} \quad \text{(A-20)}$$

$$H_{\theta,i}^{(II)}\big|_{r=R_{3,\mathrm{i}}}=H_\theta^{(III)}\big|_{r=R_{3,\mathrm{i}}} \quad \text{(A-21)}$$

$$A_i^{(II)}\big|_{r=R_{3,\mathrm{i}}}=A_i^{(III)}\big|_{r=R_{3,\mathrm{i}}} \quad \text{(A-22)}$$

$$H_\theta^{(III)}\big|_{r=R_{4,\mathrm{i}}}=H_{\theta,i}^{(IV)}\big|_{r=R_{4,\mathrm{i}}} \quad \text{(A-23)}$$

$$A_i^{(III)}\big|_{r=R_{4,\mathrm{i}}}=A_i^{(IV)}\big|_{r=R_{4,\mathrm{i}}} \quad \text{(A-24)}$$

$$H_{\theta,\mathrm{i}}^{(IV)}\big|_{r=R_5}=H_\theta^{(V)}\big|_{r=R_5} \quad \text{(A-25)}$$

$$B_{r,\mathrm{i}}^{(IV)}\big|_{r=R_5}=B_r^{(V)}\big|_{r=R_5} \quad \text{(A-26)}$$

At the interface (I-II) between the inner rotor PM subdomain and the inner air-gap subdomains the following expressions can be derived (A-27) – (A-30) using (A-7), (A-15) and boundary equations (A-19), (A-20). The Fourier coefficients $\boldsymbol{C_I}, \boldsymbol{E_I}, \boldsymbol{C_{II}}, \boldsymbol{D_{II}}, \boldsymbol{E_{II}}$ and $\boldsymbol{F_{II}}$ are all column vector of length equal to $Q \cdot K$. All constant terms are defined similarly and therefore the definition of only $\boldsymbol{G_1}$ is provided below. Same applies for the magnetization column vectors that are defined as $\boldsymbol{M_{rck}^{(I)}}$ (A-37).

$$\boldsymbol{I_{KQ}C_I}+\boldsymbol{G_1C_{II}}+\boldsymbol{G_2D_{II}}=0 \quad \text{(A-27)}$$

$$\boldsymbol{I_{KQ}E_I}+\boldsymbol{G_1E_{II}}+\boldsymbol{G_2F_{II}}=0 \quad \text{(A-28)}$$

$$\boldsymbol{G_3C_I}+\boldsymbol{I_{KQ}C_{II}}=\boldsymbol{G_{13}}\cdot\boldsymbol{M_{rck}^{(I)}} \quad \text{(A-29)}$$

$$\boldsymbol{G_3E_I}+\boldsymbol{I_{KQ}E_{II}}=\boldsymbol{G_{13}}\cdot\boldsymbol{M_{rsk}^{(I)}} \quad \text{(A-30)}$$

where

$$\boldsymbol{I_{KQ}}=diag(1,1,\dots,1)_{KQ\times KQ} \quad \text{(A-31)}$$

$$\boldsymbol{G_1}=diag(\boldsymbol{g_1}(1),\boldsymbol{g_1}(2),\dots,\boldsymbol{g_1}(\mathrm{Q}))_{QK\times QK} \quad \text{(A-32)}$$

$$\boldsymbol{g_1}(\mathbf{i})=\boldsymbol{I_K}\cdot\left(-\frac{R_2}{k}\frac{U_k(R_2,R_{3,\mathrm{i}})}{Q_k(R_2,R_{3,\mathrm{i}})}\right) \quad \text{(A-33)}$$

$$\boldsymbol{g_2}(\mathbf{i})=\boldsymbol{I_K}\cdot\left(-\frac{R_{3,\mathrm{i}}}{k}\frac{2}{Q_k(R_{3,\mathrm{i}},R_2)}\right) \quad \text{(A-34)}$$

$$\boldsymbol{g_3}(\mathbf{i})=\boldsymbol{I_K}\cdot\left(-\frac{k}{R_2}\frac{Q_k(R_2,R_1)}{U_k(R_2,R_1)}\right) \quad \text{(A-35)}$$

$$\boldsymbol{g_{13}}(\boldsymbol{i})=\boldsymbol{I_K}\left(1-\left(\frac{R_1}{R_2}\right)^{k+1}-\frac{k}{R_2}\frac{Q_k(R_2,R_1)}{U_k(R_2,R_1)}\cdot\left(1+\frac{1}{k}\left(\frac{R_1}{R_2}\right)^{k+1}\right)R_2\right) \quad \text{(A-36)}$$

$$\boldsymbol{M_{rck}^{(I)}}=\left[\boldsymbol{m_{rck}^{(I)}}(1),\boldsymbol{m_{rck}^{(I)}}(2),\dots,\boldsymbol{m_{rck}^{(I)}}(Q)\right]^{\boldsymbol{T}} \quad \text{(A-37)}$$

$$\boldsymbol{m_{rck}^{(I)}}(\mathbf{i})=\left[m_{rck}^{(I)}(1),m_{rck}^{(I)}(2),\dots,m_{rck}^{(I)}(K)\right] \quad \text{(A-38)}$$

Algebraic manipulation of (A-15), (A-17) and boundary conditions (A-21), (A-22) lead to the following relationships

at the inner air-gap and slot subdomains interface (II-III). The Fourier coefficients $\boldsymbol{E_{III}}, \boldsymbol{F_{III}}$ are column vectors of length $M \cdot Q$ and $\boldsymbol{C_{III}}, \boldsymbol{D_{III}}$ of length equal to $Q$.

$$-\boldsymbol{I_{Ki\,R3}}\boldsymbol{D_{II}} + \boldsymbol{\delta_i^T}\boldsymbol{D_{III}} + \boldsymbol{\eta_i^T}\boldsymbol{f_m}\boldsymbol{G_4}\boldsymbol{E_{III}} - \boldsymbol{\eta_i^T}\boldsymbol{f_m}\boldsymbol{G_5}\boldsymbol{F_{III}} = 0 \tag{A-39}$$

$$-\boldsymbol{I_{Ki\,R3}}\boldsymbol{F_{II}} + \boldsymbol{\sigma_i^T}\boldsymbol{D_{III}} + \boldsymbol{\xi_i^T}\boldsymbol{f_m}\boldsymbol{G_4}\boldsymbol{E_{III}} - \boldsymbol{\xi_i^T}\boldsymbol{f_m}\boldsymbol{G_5}\boldsymbol{F_{III}} = 0 \tag{A-40}$$

$$\boldsymbol{\delta_{i,\pi}}\boldsymbol{G_6}\boldsymbol{C_{II}} + \boldsymbol{\delta_{i,\pi}}\boldsymbol{G_7}\boldsymbol{D_{II}} + \boldsymbol{\sigma_{i,\pi}}\boldsymbol{G_6}\boldsymbol{E_{II}} + \boldsymbol{\sigma_{i,\pi}}\boldsymbol{G_7}\boldsymbol{F_{II}} - \boldsymbol{I_Q}\boldsymbol{C_{III}} - \boldsymbol{I_Q}\ln\left(R_{3,\mathrm{i}}\right)\boldsymbol{D_{III}} = 0 \tag{A-41}$$

$$\boldsymbol{\eta_{i,\pi}}\boldsymbol{G_6}\boldsymbol{C_{II}} + \boldsymbol{\eta_{i,\pi}}\boldsymbol{G_7}\boldsymbol{D_{II}} + \boldsymbol{\xi_{i,\pi}}\boldsymbol{G_6}\boldsymbol{E_{II}} + \boldsymbol{\xi_{i,\pi}}\boldsymbol{G_7}\boldsymbol{F_{II}} - \boldsymbol{I_{MQ}}\boldsymbol{E_{III}} = 0 \tag{A-42}$$

where

$$\boldsymbol{I_{Ki\,R3}} = diag(R_{3,1}, R_{3,2}, \dots, R_{3,\mathrm{Q}})_{QK\times QK} \tag{A-43}$$

$$\delta(i,k) = \frac{1}{\pi}\int_{\theta_i}^{\theta_i+\beta_i} \cos(k\theta)d\theta \tag{A-44}$$

$$\boldsymbol{\delta_i} = \left(\delta(i,k), \delta(i,k), \dots, \delta(i,k)\right)_{Q\times QK} \tag{A-45}$$

$$\boldsymbol{\delta_{i,\pi}} = diag\left(\frac{\pi}{\beta_i}\delta(1,k), \frac{\pi}{\beta_i}\delta(2,k), \dots, \frac{\pi}{\beta_i}\delta(Q,k)\right)_{Q\times QK} \tag{A-46}$$

$$\sigma(i,k) = \frac{1}{\pi}\int_{\theta_i}^{\theta_i+\beta_i} \sin(k\theta)d\theta \tag{A-47}$$

$$\eta(m,k,i) = \frac{1}{\pi}\int_{\theta_i}^{\theta_i+\beta_i} \cos(k\theta) \cdot \cos\left(f_{m,i}(\theta-\theta_i)\right)d\theta \tag{A-48}$$

$$\boldsymbol{\eta_i} = \begin{bmatrix} \eta(m,k,1) & \cdots & \eta(m,k,1) \\ \vdots & \ddots & \vdots \\ \eta(m,k,Q) & \cdots & \eta(m,k,Q) \end{bmatrix}_{QM\times QK} \tag{A-49}$$

$$\boldsymbol{\eta_{i,\pi}} = diag\left(\frac{2\pi}{\beta_i}\boldsymbol{\eta}(m,k,1), \frac{2\pi}{\beta_i}\boldsymbol{\eta}(m,k,2), \dots, \frac{2\pi}{\beta_i}\boldsymbol{\eta}(m,k,\mathrm{Q})\right)_{QM\times QK} \tag{A-50}$$

$$\xi(m,k,i) = \frac{1}{\pi}\int_{\theta_i}^{\theta_i+\beta_i} \sin(k\theta) \cdot \cos\left(f_{m,i}(\theta-\theta_i)\right)d\theta \tag{A-51}$$

$$\boldsymbol{f_{m,i}} = f_{m,i}\cdot\boldsymbol{I_M} \tag{A-52}$$

$$\boldsymbol{f_m} = diag\left(\boldsymbol{f_{m,i}}(1), \boldsymbol{f_{m,i}}(2), \dots, \boldsymbol{f_{m,i}}(Q)\right) \tag{A-53}$$

$$\boldsymbol{G_4} = diag(\boldsymbol{g_4}(1), \boldsymbol{g_4}(2), \dots, \boldsymbol{g_4}(Q))_{QM\times QM} \tag{A-54}$$

$$\boldsymbol{g_4}(\boldsymbol{i}) = \boldsymbol{I_M}\cdot\left(\frac{U_{f_{m,i}}\left(R_{3,\mathrm{i}}, R_{4,\mathrm{i}}\right)}{Q_{f_{m,i}}\left(R_{3,\mathrm{i}}, R_{4,\mathrm{i}}\right)}\right) \tag{A-55}$$

$$\boldsymbol{g_5}(\boldsymbol{i}) = \boldsymbol{I_M}\cdot\left(\frac{2}{Q_{f_{m,i}}\left(R_{3,\mathrm{i}}, R_{4,\mathrm{i}}\right)}\right) \tag{A-56}$$

$$\boldsymbol{g_6}(\boldsymbol{i}) = \boldsymbol{I_K}\cdot\left(\frac{R_2}{k}\frac{2}{Q_k\left(R_2, R_{3,\mathrm{i}}\right)}\right) \tag{A-57}$$

$$\boldsymbol{g_7}(\boldsymbol{i}) = \boldsymbol{I_K}\cdot\left(\frac{R_{3,\mathrm{i}}}{k}\frac{U_k\left(R_{3,\mathrm{i}}, R_2\right)}{Q_k\left(R_{3,\mathrm{i}}, R_2\right)}\right) \tag{A-58}$$

Similar to the interface with the inner air-gap subdomains, the interface (III-IV) between the outer air-gap and the slot subdomains is described as in (A-59) – (A-62) using (A-16), (A-17) and boundary equations (A-23), (A-24).

$$-\boldsymbol{I_{Ki\,R4}}\boldsymbol{C_{IV}} + \boldsymbol{\delta_i^T}\boldsymbol{D_{III}} + \boldsymbol{\eta_i^T}\boldsymbol{f_m}\boldsymbol{G_5}\boldsymbol{E_{III}} - \boldsymbol{\eta_i^T}\boldsymbol{f_m}\boldsymbol{G_4}\boldsymbol{F_{III}} = 0 \tag{A-59}$$

$$-\boldsymbol{I_{Ki\,R4}}\boldsymbol{E_{IV}} + \boldsymbol{\sigma_i^T}\boldsymbol{D_{III}} + \boldsymbol{\xi_i^T}\boldsymbol{f_m}\boldsymbol{G_5}\boldsymbol{E_{III}} - \boldsymbol{\xi_i^T}\boldsymbol{f_m}\boldsymbol{G_4}\boldsymbol{F_{III}} = 0 \tag{A-60}$$

$$\boldsymbol{\delta_{i,\pi}}\boldsymbol{G_8}\boldsymbol{C_{IV}} + \boldsymbol{\delta_{i,\pi}}\boldsymbol{G_9}\boldsymbol{D_{IV}} + \boldsymbol{\sigma_{i,\pi}}\boldsymbol{G_8}\boldsymbol{E_{IV}} + \boldsymbol{\sigma_{i,\pi}}\boldsymbol{G_9}\boldsymbol{F_{IV}} - \boldsymbol{I_Q}\boldsymbol{C_{III}} - \boldsymbol{I_Q}\ln\left(R_{4,\mathrm{i}}\right)\boldsymbol{D_{III}} = 0 \tag{A-61}$$

$$\boldsymbol{\eta_{i,\pi}}\boldsymbol{G_8}\boldsymbol{C_{IV}} + \boldsymbol{\eta_{i,\pi}}\boldsymbol{G_9}\boldsymbol{D_{IV}} + \boldsymbol{\xi_{i,\pi}}\boldsymbol{G_8}\boldsymbol{E_{IV}} + \boldsymbol{\xi_{i,\pi}}\boldsymbol{G_9}\boldsymbol{F_{IV}} - \boldsymbol{I_{MQ}}\boldsymbol{F_{III}} = 0 \tag{A-62}$$

where

$$\boldsymbol{g_8}(\boldsymbol{i}) = \boldsymbol{I_K}\cdot\left(\frac{R_{4,i}}{k}\frac{U_k\left(R_{4,i}, R_5\right)}{Q_k\left(R_{4,i}, R_5\right)}\right) \tag{A-63}$$

$$\boldsymbol{g_9(i)} = \boldsymbol{I_K} \cdot \left( \frac{R_5}{k} \frac{2}{Q_k(R_5, R_{4,i})} \right) \tag{A-64}$$

The equations at the interface (IV-V) between the outer air-gap subdomains and the outer rotor PM region can be derived adopting the same approach as for the inner rotor using the general solutions (A-8), (A-16) and boundary equations (A-25), (A-26). The Fourier coefficients $\boldsymbol{C_{IV}, D_{IV}, E_{IV}, F_{IV}, C_V}$ and $\boldsymbol{E_V}$ are column vectors of length $Q \cdot K$ and they are described as:

$$\boldsymbol{I_{KQ} C_V + G_{10} C_{IV} + G_{11} D_{IV}} = 0 \tag{A-65}$$

$$\boldsymbol{I_{KQ} E_V + G_{10} E_{IV} + G_{11} F_{IV}} = 0 \tag{A-66}$$

$$\boldsymbol{G_{12} C_V + I_{KQ} C_{IV} = G_{14} \cdot M_{rck}^{(V)}} \tag{A-67}$$

$$\boldsymbol{G_{12} E_V + I_{KQ} E_{IV} = G_{14} \cdot M_{rsk}^{(V)}} \tag{A-68}$$

where

$$\boldsymbol{g_{10}(i)} = \boldsymbol{I_K} \cdot \left( -\frac{R_{4,i}}{k} \frac{2}{Q_k(R_{4,i}, R_5)} \right) \tag{A-69}$$

$$\boldsymbol{g_{11}(i)} = \boldsymbol{I_K} \cdot \left( -\frac{R_5}{k} \frac{U_k(R_5, R_{4,i})}{Q_k(R_5, R_{4,i})} \right) \tag{A-70}$$

$$\boldsymbol{g_{12}(i)} = \boldsymbol{I_K} \cdot \left( -\frac{k}{R_5} \frac{Q_k(R_5, R_6)}{U_k(R_5, R_6)} \right) \tag{A-71}$$

$$\begin{aligned} \boldsymbol{g_{14}(i)} = \boldsymbol{I_K} \Bigg( & 1 - \left(\frac{R_6}{R_5}\right)^{k+1} - \frac{k}{R_5} \frac{Q_k(R_5, R_6)}{U_k(R_5, R_6)} \\ & \cdot \left( 1 + \frac{1}{k} \left(\frac{R_6}{R_5}\right)^{k+1} \right) R_5 \Bigg) \end{aligned} \tag{A-72}$$

The torque on each rotor is calculated using the Maxwell's Stress Tensor along a contour in each air-gap (A-73). The accuracy of the torque calculation where large asymmetries exist is maximized by taking an average of the torque calculations for *s = i* and *s = i-1* as per (A-17).

$$\begin{aligned} T = \frac{L \cdot R_{air-gap}^2}{\mu_0} \int_0^{2\pi} & B_r^{(II/IV)}(R_{air-gap}, \theta) \\ & \cdot B_\theta^{(II/IV)}(R_{air-gap}, \theta) \cdot d\theta \end{aligned} \tag{A-73}$$

Considering the expressions for $B_r^{(II/IV)}$ and $B_\theta^{(II/IV)}$, equation (A-73) can be expanded to the following:

$$\begin{aligned} T = \frac{L \cdot R_{air-gap}^2}{\mu_0} \Bigg( & \sum_{i=1}^{Q} \Bigg( \sum_{k=1}^{2K} \sum_{l=1}^{k} O_{II,i,k} \cdot V_{II,i,j} \\ & - \sum_{k=1}^{K} \sum_{l=K+1}^{2K-k+1} O_{II,i,k} \cdot V_{II,i,l} \Bigg) \Bigg) \end{aligned} \tag{A-74}$$

where,

$$j = k - l + 1 \tag{A-75}$$

$$\begin{aligned} O_{II,i,k} = -\Bigg( & C_{II,i,k} \frac{R_2}{r} \frac{U_k(r, R_{3,i})}{Q_k(R_2, R_{3,i})} \\ & + D_{II,i,k} \frac{R_{3,i}}{r} \frac{U_k(r, R_2)}{Q_k(R_{3,i}, R_2)} \Bigg) \\ & \cdot \int_{\theta_i}^{\theta_{i+1}} sin(k\theta)\, d\theta \\ & + \Bigg( E_{II,i,k} \frac{R_2}{r} \frac{U_k(r, R_{3,i})}{Q_k(R_2, R_{3,i})} \\ & + F_{II,i,k} \frac{R_{3,i}}{r} \frac{U_k(r, R_2)}{Q_k(R_{3,i}, R_2)} \Bigg) \\ & \cdot \int_{\theta_i}^{\theta_{i+1}} cos(k\theta)\, d\theta \end{aligned} \tag{A-76}$$

$$\begin{aligned} V_{II,i,j} = -\Bigg( & C_{II,i,j} \frac{R_2}{r} \frac{Q_k(r, R_{3,i})}{Q_k(R_2, R_{3,i})} \\ & + D_{II,i,j} \frac{R_{3,i}}{r} \frac{Q_k(r, R_2)}{Q_k(R_{3,i}, R_2)} \Bigg) \\ & \cdot \int_{\theta_i}^{\theta_{i+1}} \cos(j\theta)\, d\theta \\ & + \Bigg( E_{II,i,j} \frac{R_2}{r} \frac{Q_k(r, R_{3,i})}{Q_k(R_2, R_{3,i})} \\ & + F_{II,i,j} \frac{R_{3,i}}{r} \frac{Q_k(r, R_2)}{Q_k(R_{3,i}, R_2)} \Bigg) \\ & \cdot \int_{\theta_i}^{\theta_{i+1}} \sin(j\theta)\, d\theta \end{aligned} \tag{A-77}$$

## REFERENCES


[1] K. Atallah and D. Howe, "A novel high-performance magnetic gear," in *IEEE Transactions on Magnetics*, 2001, vol. 37, no. 4 I, pp. 2844–2846.

[2] V. Asnani, J. Scheidler, and T. Tallerico, "Magnetic gearing research at NASA," *Annu. Forum Proc. - AHS Int.*, vol. 2018-May, 2018.

[3] L. Shah, A. Cruden, and B. W. Williams, "A magnetic gear box for application with a contra-rotating tidal turbine," *Proc. Int. Conf. Power Electron. Drive Syst.*, pp. 989–993, 2007.

[4] R. Z. A. Borisavljevic, J. W. Jansen, and E. A. Lomonova, "Modeling , Design and Experimental Validation of a Small-Sized Magnetic Gear," no. 2, pp. 560–565, 2013.

[5] J. X. Shen, H. Y. Li, H. Hao, and M. J. Jin, "A Coaxial Magnetic Gear With Consequent-Pole Rotors," *IEEE Trans. Energy Convers.*, vol. 32, no. 1, pp. 267–275, 2017.

[6] L. Jian, S. Member, K. T. Chau, and S. Member, "A Coaxial Magnetic Gear With Halbach Permanent-Magnet Arrays," *IEEE Trans. Energy Convers.*, vol. 25, no. 2, pp. 319–328, 2010.

[7] X. Yin, P. D. Pfister, and Y. Fang, "A Novel Magnetic Gear: Toward a Higher Torque Density," *IEEE Trans. Magn.*, vol. 51, no. 11, pp. 1–4, 2015.

[8] X. Li, K. T. Chau, M. Cheng, W. Hua, and Y. Du, "An improved coaxial magnetic gear using flux focusing," *2011 Int. Conf. Electr. Mach. Syst. ICEMS 2011*, no. d, pp. 2–5, 2011.

[9] M. Filippini and P. Alotto, "Coaxial magnetic gears design and optimization," *IEEE Trans. Ind. Electron.*, vol. 64, no. 12, pp. 1–1, 2017.

[10] P. O. Rasmussen, T. O. Andersen, F. T. Jørgensen, and O. Nielsen, "Development of a high-performance magnetic gear," *IEEE Trans. Ind. Appl.*, vol. 41, no. 3, pp. 764–770, 2005.

[11] J. Rens, K. Atallah, S. D. Calverley, and D. Howe, "A novel magnetic harmonic gear," *IEEE Trans. Ind. Appl.*, vol. 46, no. 1, pp. 206–212, 2010.

[12] F. T. Jørgensen, T. O. Andersen, and P. O. Rasmussen, "The cycloid permanent magnetic gear," *IEEE Trans. Ind. Appl.*, vol. 44, no. 6, pp. 1659–1665, 2008.

[13] Cheng-Chi Huang, Mi-Ching Tsai, D. G. Dorrell, and Bor-Jeng Lin, "Development of a Magnetic Planetary Gearbox," *IEEE Trans. Magn.*, vol. 44, no. 3, pp. 403–412, 2008.

[14] K. Atallah, S. D. Calverley, and D. Howe, "Design, analysis and realisation of a high-performance magnetic gear," *IEE Proceedings-Electric Power Appl.*, vol. 151, no. 2, pp. 135–143, 2004.

[15] S. Gerber and R. J. Wang, "Analysis of the end-effects in magnetic gears and magnetically geared machines," *Proc. - 2014 Int. Conf. Electr. Mach. ICEM 2014*, pp. 396–402, 2014.

[16] A. Matthee, S. Gerber, and R. Wang, "A high performance concentric magnetic gear," *Proc. - South. African Univ. Power Eng. Conf. 2015*, pp. 203–207, 2015.

[17] A. Matthee, R.-J. Wang, C. J. Agenbach, D. N. J. Els, and M. J. Kamper, "Evaluation of a magnetic gear for air-cooled condenser applications," *IET Electr. Power Appl.*, vol. 12, no. 5, pp. 677–683, 2018.

[18] X. Liu, K. T. Chau, J. Z. Jiang, and C. Yu, "Design and analysis of interior-magnet outer-rotor concentric magnetic gears," *J. Appl. Phys.*, vol. 105, no. 7, pp. 103–106, 2009.

[19] S. Gerber and R. J. Wang, "Evaluation of a prototype magnetic gear," *Proc. IEEE Int. Conf. Ind. Technol.*, pp. 319–324, 2013.

[20] A. Leontaritis, A. Nassehi, and J. M. Yon, "Causes and effects of Geometric Deviation in Magnetic Gears," in *Proc. IEEE Workshop on Electrical Machines Design Control and Diagnosis (WEMDCD 2019)*, 2019, pp. 34–39.

[21] A. Leontaritis, A. Nassehi, and J. M. Yon, "Assessing the Effect of Geometric Error on the Performance of Magnetic Gears," in *Proc. IEEE Int. Electrical Machines & Drives Conf. (IEMDC 19)*, 2019, pp. 1951–1958.

[22] T. Lubin, S. Mezani, and A. Rezzoug, "Analytical computation of the magnetic field distribution in a magnetic gear," *IEEE Trans. Magn.*, vol. 46, no. 7, pp. 2611–2621, 2010.

[23] X. Zhang, X. Liu, Z. Song, and Z. Chen, "Fast calculation of magnetic field distribution in magnetic gear for high torque application," *2016 XXII International Conference on Electrical Machines (ICEM)*. pp. 1742–1748, 2016.

[24] B. Dianati, H. Heydari, and S. A. Afsari, "Analytical Computation of Air-Gap Magnetic Field in a Viable Superconductive Magnetic Gear," *IEEE Trans. Appl. Supercond.*, vol. 26, no. 6, 2016.

[25] A. Penzkofer and K. Atallah, "Scaling of Pseudo Direct Drives for Wind Turbine Application," *IEEE Trans. Magn.*, vol. 52, no. 7, pp. 1–5, 2016.

[26] H. Y. Li, H. Hao, M. J. Jin, and J. X. Shen, "Analytical Calculation of Magnetic Field Distribution in Magnetic Gears with Consequent-Pole Rotors by Subdomain Method," *2016 IEEE Veh. Power Propuls. Conf. VPPC 2016 - Proc.*, pp. 1–6, 2016.

[27] A. Penzkofer and K. Atallah, "Magnetic gears for high torque applications," *IEEE Trans. Magn.*, vol. 50, no. 11, 2014.

[28] A. Pina, S. Paul, R. Islam, and L. Xu, "Analytical Model for Predicting Effects of Manufacturing Variations on Cogging Torque in Surface-Mounted Permanent Magnet Motors," *IEEE Trans. Ind. Appl.*, vol. PP, no. 99, p. 1, 2016.

[29] D. Meeker, "FEMM." 2012.

[30] M. Desvaux, B. Traullé, R. Le Goff Latimier, S. Sire, B. Multon, and H. Ben Ahmed, "Computation Time Analysis of the Magnetic Gear Analytical Model," *IEEE Trans. Magn.*, vol. 53, no. 5, 2017.

[31] K. K. Uppalapati and J. Z. Bird, "An Iterative Magnetomechanical Deflection Model for a Magnetic Gear," *IEEE Trans. Magn.*, vol. 50, no. 2, pp. 4–7, 2014.

[32] M. Desvaux, B. Multon, H. Ben Ahmed, and S. Sire, "Supporting the laminated ferromagnetic pole pieces in a magnetic gear: A structure behaviour analysis from a multibody model," *Mech. Mach. Sci.*, vol. 54, pp. 85–94, 2018.

[33] T. P. Burke, "Kernel Density Estimation Techniques for Monte Carlo Reactor Analysis," 2016.

[34] B. W. Silverman, *Density estimation: For statistics and data analysis*. London: Chapman and Hall, 1986.

[35] The Mathworks Inc., "MATLAB - MathWorks," *www.mathworks.com/products/matlab*, 2016. [Online]. Available: http://www.mathworks.com/products/matlab/.

[36] A. W. Bowman and A. Azzalini, *Applied Smoothing Techniques for Data Analysis*. New York: Oxford University Press Inc., 1997.

[37] V. Epanechnikov, "Nonparametric estimation of a multidimensional probability density," *Theory Probab. Its Appl.*, 1969.

[38] G. J. Hahn, "Sample Sizes for Monte Carlo Simulation.," *IEEE Trans. Syst. Man Cybern.*, vol. SMC-2, no. 5, pp. 678–680, 1972.

[39] A. Hawksworth, "Pole-Piece Structure for a Magnetic Gear," US Patent Number 2017/0005559 A1, 2017.